

Decomposing Normal and Abnormal Features of Medical Images for Content-based Image Retrieval

Kazuma Kobayashi

National Cancer Center Research Institute, Japan

Ryuichiro Hataya

Graduate School of Information Science and Technology, The University of Tokyo, Japan

Yusuke Kurose

Tatsuya Harada

Research Center for Advanced Science and Technology, The University of Tokyo, Japan

Ryuji Hamamoto

National Cancer Center Research Institute, Japan

KAZUMKOB@NCC.GO.JP

HATAYA@NLAB.CI.I.U-TOKYO.AC.JP

KUROSE@MI.T.U-TOKYO.AC.JP

HARADA@MI.T.U-TOKYO.AC.JP

RHAMAMOT@NCC.GO.JP

Abstract

Medical images can be decomposed into normal and abnormal features, which is considered as the *compositionality*. Based on this idea, we propose an encoder-decoder network to decompose a medical image into two discrete latent codes: a *normal anatomy code* and an *abnormal anatomy code*. Using these latent codes, we demonstrate a similarity retrieval by focusing on either normal or abnormal features of medical images.

Keywords: Decomposed feature representation; Content-based image retrieval; Medical imaging

1. Introduction

In medical imaging, the characteristics purely derived from a disease should reflect the extent to which abnormal findings deviate from the normal features that would have existed. Indeed, physicians often need corresponding normal images without abnormal findings of interest or, conversely, images that contain similar abnormal findings regardless of normal anatomical context. This is called comparative diagnostic reading of medical images, which is essential for a cor-

rect diagnosis. To support the comparative diagnostic reading, content-based image retrieval (CBIR) utilizing either normal or abnormal features will be useful.

Here, we define this two-tiered nature of normal and abnormal features as the *compositionality* of medical images. Subsequently, we consider a method to decompose a medical image into two low-dimensional representations, where the two latent codes representing normal and abnormal anatomies should be collective for reconstructing the original image (Figure 1).

To our best knowledge, few studies have focused on the compositionality of medical images. Recently, image-to-image translation techniques mainly derived from CycleGAN (Zhu et al., 2017) were exploited to disentangle the domain-specific variations of medical images (Xia et al., 2020; Liao et al., 2020; Vorontsov et al., 2019). For example, Tian et al. successfully transformed an input image with pathology into a normal-appearing image by leveraging several cycle-consistency losses (Xia et al., 2020). However, these approaches did not treat the compositionality in a separable manner, i.e., the

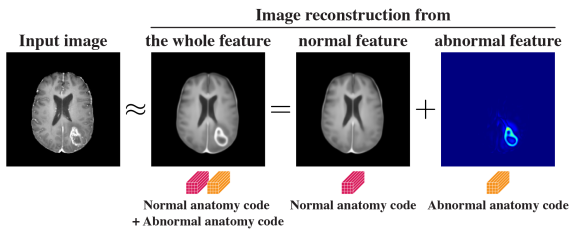


Figure 1: Our concept of the compositionality of medical images, indicating that the entire image should be composed of the representation of normal and abnormal features.

latent spaces of these methods were not explicitly designed for down-stream tasks.

In this paper, we propose an encoder-decoder network to project a medical image into a pair of latent spaces, each of which produces a *normal anatomy code* and an *abnormal anatomy code*. Using these latent codes, our CBIR framework can retrieve images by focusing on either normal or abnormal features, providing excellent performances in qualitative evaluations.

2. Methodology

The proposed network consists of an encoder and two decoders, a segmentation decoder and an image decoder (Figure 2). A pair of discrete latent spaces exists at the bottom that produces normal and abnormal anatomy codes, separately. See Appendix A for the details of the network architecture.

Feature encoding: The encoder uses a two-dimensional medical image $\mathbf{x} \in \mathbb{R}^{C \times H \times W}$ as an input and maps it into two latent representations, $\mathbf{z}_e^- \in \mathbb{R}^{D \times H' \times W'}$ and $\mathbf{z}_e^+ \in \mathbb{R}^{D \times H' \times W'}$, where \mathbf{z}_e^- and \mathbf{z}_e^+ correspond to the features of normal and abnormal anatomies, respectively. We used \mathbf{z}_e^\mp to represent both features. Subsequently, vector quantization was used to discretize \mathbf{z}_e^\mp . Namely, each elemental vector $\mathbf{z}_{e_k}^\mp \in \mathbb{R}^D$ was

replaced with the closest code vector in each codebook $\mathbf{e}^\mp \in \mathbb{R}^{D \times K}$ comprising K code vectors. The codebooks were updated as VQ-VAEs (van den Oord et al., 2017; Razavi et al., 2019). We denote the quantized vector of \mathbf{z}_e^\mp as \mathbf{z}_q^\mp . Here, \mathbf{z}_q^- is referred to as the normal anatomy code, and \mathbf{z}_q^+ as the abnormal anatomy code.

Feature decoding: The segmentation decoder uses abnormal anatomy code \mathbf{z}_q^+ as input and outputs segmentation label $\hat{\mathbf{y}} \in \mathbb{R}^{C' \times H \times W}$. Meanwhile, the image decoder f performs conditional image generation using the *spatially-adaptive normalization* (SPADE) (Park et al., 2019). SPADE is designed to propagate semantic layouts to the process of synthesizing images (Appendix B). The image decoder uses the normal anatomy code \mathbf{z}_q^- as its primary input. When the image decoder is encouraged to reconstruct the entire input image $\hat{\mathbf{x}}^+$, the logit of the segmentation decoder $\tilde{\mathbf{y}}$ is transmitted to each layer of the image decoder via the SPADE modules ($f(\mathbf{z}_q^-, \tilde{\mathbf{y}}) = \hat{\mathbf{x}}^+$). When *null* information, where $\tilde{\mathbf{y}}$ is filled with 0s, is propagated to the SPADE modules, normal-appearing image $\hat{\mathbf{x}}^-$ is generated by the image decoder ($f(\mathbf{z}_q^-, \mathbf{0}) = \hat{\mathbf{x}}^-$).

Learning objectives: We defined several loss functions (see Appendix C for the details): latent loss L_{lat} for optimizing the encoder and the codebooks, discrimination loss L_{dis} for the encoder to identify the presence of abnormality, segmentation loss L_{seg} for the segmentation decoder, reconstruction loss L_{rec} , and residual loss L_{res} for the conditioned image generation performed in coordination between the two decoders. The overall objective can be summarized as follows: $L_{\text{total}} = L_{\text{lat}} + \lambda_1 L_{\text{dis}} + \lambda_2 L_{\text{seg}} + \lambda_3 L_{\text{rec}} + \lambda_4 L_{\text{res}}$, where λ s are used for balancing the terms. The details of learning configuration and an example of the model training result are presented in Appendix D and Appendix E, respectively.

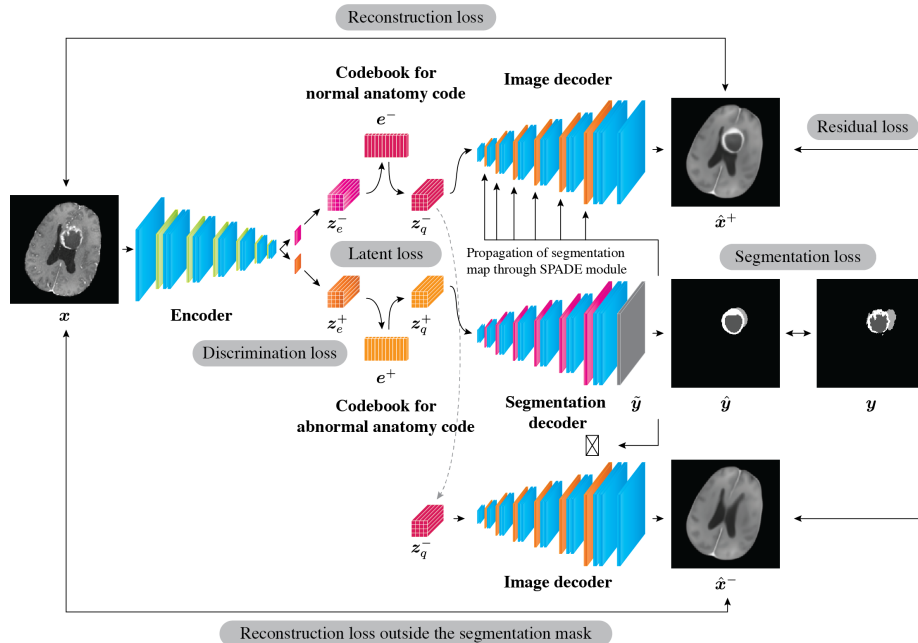


Figure 2: Schematic of the proposed encoder-decoder network.

Content-based image retrieval: After the training, the encoder learned to decompose medical images into normal and abnormal anatomy codes. We defined three measurements according to the types of latent codes as follows: D_{normal}^- for normal anatomy codes, D_{abnormal}^+ for abnormal anatomy codes, and D_{concat} for concatenated codes of the two codes. The L2 distance was calculated between the query and reference latent codes (see Appendix F for the overview of the proposed CBIR method).

3. Dataset

We used brain magnetic resonance (MR) images with gliomas from the 2019 BraTS Challenge (Menze et al., 2015; Bakas et al., 2017; Bakas S et al., 2017a,b), containing a training dataset with 355 patients, a validation dataset with 125 patients, and a test dataset with 167 patients. Among T1, gadolinium (Gd)-enhancing T1, T2, and FLAIR sequences, only the Gd-enhanced T1-

weighted sequence was used. The training dataset contained three segmentation labels of abnormality: Gd-enhancing tumor (ET), peritumoral edema (ED), and necrotic and non-enhancing tumor core (TC). We used the training dataset to train the networks. Further, each image in the validation and test dataset was segmented into six normal anatomical labels (left and right cerebrum, cerebellum, and ventricles) and three abnormal labels (ET, ED, and TC). The validation and test datasets were used as query and reference datasets, respectively, for the performance evaluation of CBIR.

4. Results

Example CBIR results showing 5 images with the closest latent codes based on D_{normal}^- , D_{abnormal}^+ , and D_{concat} are presented in Figure 3. Distance calculation based on normal anatomy codes D_{normal}^- retrieved images with similar normal anatomical labels irrespective of gross abnormalities (Figure

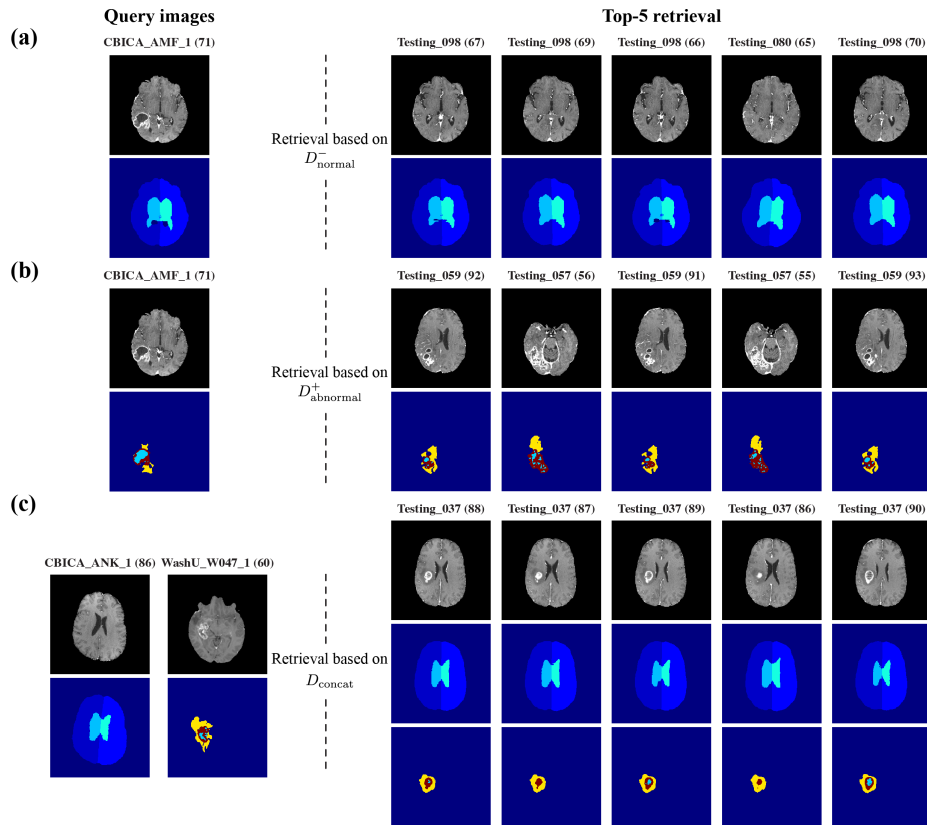


Figure 3: Example results of content-based image retrieval based on similarities of decomposed latent codes. Images are shown with normal or abnormal anatomical labels that are corresponded to the semantics utilized in the retrieval. Although the image retrieval employed latent codes instead of label information, the retrieved images accompanied similar labels to those of the query images. Patient identifiers with slice numbers are noted.

3a). Distance calculation based on abnormal anatomy codes $D_{abnormal}^+$ retrieved images with similar abnormal anatomical labels (Figure 3b). Note that the variety of normal anatomical contexts of the retrieved images. In the calculation using D_{concat} , the query latent code was made from a combination of the normal anatomy code of the left image (CBICA_ANK_1) and the abnormal anatomy code of the right image (WashU_W047_1) (Figure 3c). Note that normal anatomies and abnormal anatomies of the retrieved images

resemble those of the left query image and right query image, respectively.

5. Conclusion

We demonstrated the CBIR algorithm focusing on the semantic composites of medical imaging. This application can be useful to support comparative diagnostic reading, which is essential for a correct diagnosis. We will further evaluate the quantitative performance of the proposed method.

Acknowledgments

We are grateful to Dr. Ken Asada, Dr. Ryo Shimoyama, and Dr. Mototaka Miyake for helpful discussions. The authors thank the members of the Division of Molecular Modification and Cancer Biology of the National Cancer Center Research Institute for their kind support. The RIKEN AIP Deep Learning Environment (RAIDEN) supercomputer system was used in this study to perform computations.

Funding: This work was supported by JST CREST (Grant Number JP-MJCR1689), JST AIP-PRISM (Grant Number JPMJCR18Y4), and JSPS Grant-in-Aid for Scientific Research on Innovative Areas (Grant Number JP18H04908).

Competing interests: Kazuma Kobayashi and Ryuji Hamamoto have received research funding from Fujifilm Corporation.

References

- Spyridon Bakas, Hamed Akbari, Aristeidis Sotiras, Michel Bilello, Martin Rozycki, Justin S. Kirby, John B. Freymann, Keyvan Farahani, and Christos Davatzikos. Advancing The Cancer Genome Atlas glioma MRI collections with expert segmentation labels and radiomic features. *Scientific Data*, 4, 2017.
- Bakas S, Akbari H, Sotiras A, Bilello M, Rozycki M, Kirby J, Freymann J, Farahani K, and Davatzikos C. Segmentation labels and radiomic features for the pre-operative scans of the TCGA-GBM collection. *The Cancer Imaging Archive*, 2017a. doi: 10.7937/K9/TCIA.2017.KLXWJJ1Q.
- Bakas S, Akbari H, Sotiras A, Bilello M, Rozycki M, Kirby J, Freymann J, Farahani K, and Davatzikos C. Segmentation labels and radiomic features for the pre-operative scans of the TCGA-LGG collection. *The Cancer Imaging Archive*, 2017b.
- Kaiming He, Xiangyu Zhang, Shaoqing Ren, and Jian Sun. Delving deep into rectifiers: Surpassing human-level performance on imagenet classification. In *2015 IEEE International Conference on Computer Vision (ICCV)*, pages 1026–1034, 2015.
- Sergey Ioffe and Christian Szegedy. Batch normalization: Accelerating deep network training by reducing internal covariate shift. In *Proceedings of the 32nd International Conference on International Conference on Machine Learning - Volume 37*, pages 448–456, 2015.
- Diederik P. Kingma and Jimmy Ba. Adam: A method for stochastic optimization. In *The 3rd International Conference on Learning Representations (ICLR)*, 2015.
- H. Liao, W. Lin, S. K. Zhou, and J. Luo. Adn: Artifact disentanglement network for unsupervised metal artifact reduction. *IEEE Transactions on Medical Imaging*, 39(3):634–643, 2020.
- B. H. Menze, A. Jakab, S. Bauer, J. Kalpathy-Cramer, K. Farahani, J. Kirby, Y. Burren, N. Porz, J. Slotboom, R. Wiest, L. Lanczi, E. Gerstner, M. Weber, T. Arbel, B. B. Avants, N. Ayache, P. Buendia, D. L. Collins, N. Cordier, J. J. Corso, A. Criminisi, T. Das, H. Delingette, Ç. Demiralp, C. R. Durst, M. Dojat, S. Doyle, J. Festa, F. Forbes, E. Geremia, B. Glocker, P. Golland, X. Guo, A. Hamamci, K. M. Iftekharuddin, R. Jena, N. M. John, E. Konukoglu, D. Lashkari, J. A. Mariz, R. Meier, S. Pereira, D. Precup, S. J. Price, T. R. Raviv, S. M. S. Reza, M. Ryan, D. Sarikaya, L. Schwartz, H. Shin, J. Shotton, C. A. Silva, N. Sousa, N. K. Subbanna, G. Szekely, T. J. Taylor,

- O. M. Thomas, N. J. Tustison, G. Unal, F. Vasseur, M. Wintermark, D. H. Ye, L. Zhao, B. Zhao, D. Zikic, M. Prastawa, M. Reyes, and K. Van Leemput. The multimodal brain tumor image segmentation benchmark (brats). *IEEE Transactions on Medical Imaging*, 34(10):1993–2024, 2015.
- Taesung Park, Ming-Yu Liu, Ting-Chun Wang, and Jun-Yan Zhu. Semantic image synthesis with spatially-adaptive normalization. In *Proceedings of the IEEE/CVF Conference on Computer Vision and Pattern Recognition (CVPR)*, pages 2337–2346, 2019.
- Adam Paszke, Sam Gross, Francisco Massa, Adam Lerer, James Bradbury, Gregory Chanan, Trevor Killeen, Zeming Lin, Natalia Gimelshein, Luca Antiga, Alban Desmaison, Andreas Kopf, Edward Yang, Zachary DeVito, Martin Raison, Alykhan Tejani, Sasank Chilamkurthy, Benoit Steiner, Lu Fang, Junjie Bai, and Soumith Chintala. Pytorch: An imperative style, high-performance deep learning library. In *Advances in Neural Information Processing Systems 32 (NeurIPS)*, pages 8024–8035, 2019.
- Ali Razavi, Aaron van den Oord, and Oriol Vinyals. Generating diverse high-fidelity images with vq-vae-2. In *Advances in Neural Information Processing Systems 32 (NeurIPS)*, pages 14866–14876, 2019.
- Carole H. Sudre, Wenqi Li, Tom Vercauteren, Sebastien Ourselin, and M. Jorge Cardoso. Generalised dice overlap as a deep learning loss function for highly unbalanced segmentations. *Lecture Notes in Computer Science*, pages 240–248, 2017.
- Aaron van den Oord, Oriol Vinyals, and Koray Kavukcuoglu. Neural discrete representation learning. In *Advances in Neural Information Processing Systems 30 (NeurIPS)*, pages 6306–6315, 2017.
- Eugene Vorontsov, Pavlo Molchanov, Christopher Beckham, Wonmin Byeon, Shalini De Mello, Varun Jampani, Ming-Yu Liu, Samuel Kadoury, and Jan Kautz. Towards semi-supervised segmentation via image-to-image translation. *arXiv preprint arXiv:1904.01636*, 2019.
- Tian Xia, Agisilaos Chatsias, and Sotirios A. Tsaftaris. Pseudo-healthy synthesis with pathology disentanglement and adversarial learning. *Medical Image Analysis*, 64:101719, 2020.
- Zhou Wang, A. C. Bovik, H. R. Sheikh, and E. P. Simoncelli. Image quality assessment: from error visibility to structural similarity. *IEEE Transactions on Image Processing*, 13(4):600–612, 2004.
- J. Zhu, T. Park, P. Isola, and A. A. Efros. Unpaired image-to-image translation using cycle-consistent adversarial networks. In *2017 IEEE International Conference on Computer Vision (ICCV)*, pages 2242–2251, 2017.

Appendix A. Detailed Network Architecture of the Proposed Model

Table A.1 demonstrates the detailed architecture of the encoder. Table A.2 presents the shared architecture between the image and segmentation decoders. The two decoders share most of the components except for the normalization function, where the image decoder utilizes batch normalization (Ioffe and Szegedy, 2015), and the segmentation decoder exploits SPADE (Park et al., 2019).

Table A.1: The detailed architecture of the encoder.

Module	Activation	Output shape
Input image		$1 \times 256 \times 256$
Conv	$[5 \times 5 \quad 32]$	$32 \times 256 \times 256$
AvgPool	-	$32 \times 128 \times 128$
Res-block	$[3 \times 3 \quad 64]$ $[3 \times 3 \quad 64]$	$64 \times 128 \times 128$
AvgPool	-	$64 \times 64 \times 64$
Res-block	$[3 \times 3 \quad 128]$ $[3 \times 3 \quad 128]$	$128 \times 64 \times 64$
AvgPool	-	$128 \times 32 \times 32$
Res-block	$[3 \times 3 \quad 256]$ $[3 \times 3 \quad 256]$	$256 \times 32 \times 32$
AvgPool	-	$256 \times 16 \times 16$
Res-block	$[3 \times 3 \quad 512]$ $[3 \times 3 \quad 512]$	$512 \times 16 \times 16$
AvgPool	-	$512 \times 8 \times 8$
Split	$[3 \times 3 \quad 64]$, $[3 \times 3 \quad 64]$	$64 \times 8 \times 8$, $64 \times 8 \times 8$

Table A.2: Detailed architecture shared between the image and segmentation decoders.

Module	Activation	Output shape
Latent representation	-	$64 \times 8 \times 8$
Conv-block	$[3 \times 3 \quad 512]$ $[3 \times 3 \quad 512]$	$512 \times 8 \times 8$
Upsample (SPADE-)Res-block	$[3 \times 3 \quad 256]$ $[3 \times 3 \quad 256]$ $[3 \times 3 \quad 256]$	$256 \times 16 \times 16$ $256 \times 16 \times 16$
Upsample (SPADE-)Res-block	$[3 \times 3 \quad 128]$ $[3 \times 3 \quad 128]$ $[3 \times 3 \quad 128]$	$128 \times 32 \times 32$ $128 \times 32 \times 32$
Upsample (SPADE-)Res-block	$[3 \times 3 \quad 64]$ $[3 \times 3 \quad 64]$ $[3 \times 3 \quad 64]$	$64 \times 64 \times 64$ $64 \times 64 \times 64$
Upsample (SPADE-)Res-block	$[3 \times 3 \quad 32]$ $[3 \times 3 \quad 32]$ $[3 \times 3 \quad 32]$	$32 \times 128 \times 128$ $32 \times 128 \times 128$
Upsample (SPADE-)Res-block	$[3 \times 3 \quad 16]$ $[3 \times 3 \quad 16]$ $[3 \times 3 \quad 16]$	$16 \times 256 \times 256$ $16 \times 256 \times 256$
Conv	$[5 \times 5 \quad 1]$	$1 \times 256 \times 256$

Appendix B. SPADE Module for Propagation of Semantic Segmentation Map

The detailed architecture of the SPADE module is shown in Figure B.1.

Appendix C. Details of Learning Objectives

Several loss functions were designed for the training. Hereinafter, we denote by \mp to indicate that a particular term is either for the path based on the normal anatomy code ($-$) or abnormal anatomy code ($+$).

Latent loss: In the learning framework of the VQ-VAE (van den Oord et al., 2017; Razavi et al., 2019), the latent loss L_{lat} is optimized for acquiring latent embeddings for data samples. We define L_{lat} as a sum of L_{lat}^- and L_{lat}^+ for the normal and abnormal anatomy codes, respectively, as follows:

$$L_{\text{lat}}^{\mp} = \|\text{sg}[\mathbf{z}_e^{\mp}(x)] - \mathbf{e}^{\mp}\|_2^2 + \beta \|\mathbf{z}_e^{\mp}(x) - \text{sg}[\mathbf{e}^{\mp}]\|_2^2, \quad (1)$$

$$L_{\text{lat}} = L_{\text{lat}}^- + L_{\text{lat}}^+, \quad (2)$$

where sg represents the stop-gradient operator that serves as an identity function at the forward computation time and has zero partial derivatives. During the training, the *codebook loss*, which is the first term in the equation above, updates the codebook variables by transferring the selected latent codes to the output of the encoder. Additionally, the *commitment loss*, which is the second term, encourages the output of the encoder to move closer to specific latent codes.

Discrimination loss: Because the input images do not always convey abnormal findings, the encoder must be able to distinguish the abnormalities. To implement a discriminative function in the encoder, we extend the commitment loss particularly for the abnormal anatomy code. The encoder is trained to

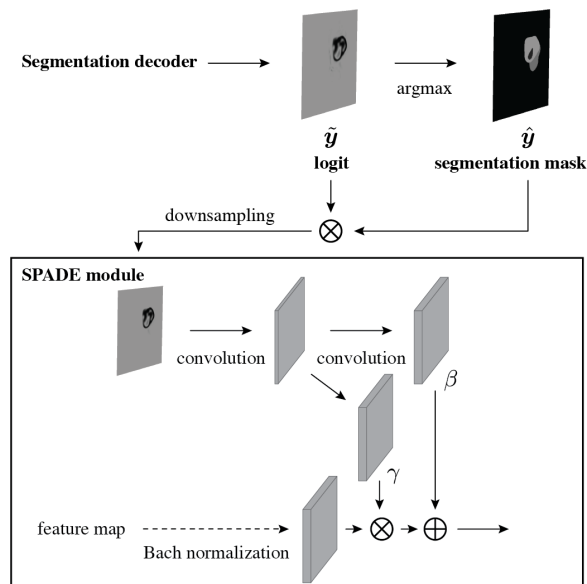


Figure B.1: Logit $\tilde{\mathbf{y}}$ applied by the segmentation mask $\hat{\mathbf{y}}$ is further downsampled to achieve resolutions corresponding to those of each layer in the image decoder. SPADE module propagates the semantic layout of abnormalities into the image generation process.

minimize the commitment loss when abnormalities exist. Meanwhile, for normal input images, the encoder is encouraged to increase the term up to a threshold value of π . We define this loss function as the *discrimination loss* for the path to the abnormal anatomy code as follows:

$$L_{\text{dis}} = \max(\pi - \|\mathbf{z}_e^+(x) - \text{sg}[\mathbf{e}^+]\|_2^2, 0), \quad (3)$$

where π is a positive scalar of the threshold.

Segmentation loss: The segmentation decoder infers the segmentation labels, which are classified as $\mathcal{K}(= 3)$ abnormal segmentation categories in the training dataset. The loss function for the output of the segmentation decoder is a composite of the generalized Dice (Sudre et al., 2017) and cross-entropy losses as follows:

$$L_{\text{dice}} = 1 - 2 \frac{\sum_{k \in \mathcal{K}} w_k |\hat{\mathbf{y}}_k \cap \mathbf{y}_k|}{\sum_{k \in \mathcal{K}} w_k (|\hat{\mathbf{y}}_k| + |\mathbf{y}_k|)}, \quad (4)$$

$$L_{\text{entropy}} = -\frac{1}{N} \sum_{k \in \mathcal{K}} \mathbf{y}_k \log \tilde{\mathbf{y}}, \quad (5)$$

$$L_{\text{seg}} = L_{\text{dice}} + L_{\text{entropy}}, \quad (6)$$

where $\tilde{\mathbf{y}}$ indicates the logit output of the segmentation decoder, N is the number of pixels, and w_k is determined as $w_k = \frac{1}{(\sum_N \mathbf{y}_k)^2}$ to mitigate the class imbalance problem.

Reconstruction loss: To guarantee a difference between two types of generated images, $\hat{\mathbf{x}}^-$ and $\hat{\mathbf{x}}^+$, we applied a pixel-wise reconstruction loss based on the region of abnormality. Suppose $\mathbf{M} \in \{0, 1\}^{C \times H \times W}$ defines the mask, indicating that pixels with any abnormality labels are set to 1 and 0 otherwise, and $\overline{\mathbf{M}}$ is the complementary set of \mathbf{M} . Briefly, \mathbf{M} presents the region of abnormality, and $\overline{\mathbf{M}}$ indicates the region of normal anatomy. Using these masks, the construc-

tion loss L_{rec} is defined as follows:

$$L_{\text{rec}}^- = \|\overline{\mathbf{M}} \odot \mathbf{x}^- - \overline{\mathbf{M}} \odot \mathbf{x}\|_2^2 + (1 - \text{SSIM}(\overline{\mathbf{M}} \odot \mathbf{x}^-, \overline{\mathbf{M}} \odot \mathbf{x})), \quad (7)$$

$$L_{\text{rec}}^+ = \|\mathbf{x}^+ - \mathbf{x}\|_2^2 + (1 - \text{SSIM}(\mathbf{x}^+, \mathbf{x})) + \|\mathbf{M} \odot \mathbf{x}^+ - \mathbf{M} \odot \mathbf{x}\|_2^2 + (1 - \text{SSIM}(\mathbf{M} \odot \mathbf{x}^+, \mathbf{M} \odot \mathbf{x})), \quad (8)$$

$$L_{\text{rec}} = L_{\text{rec}}^- + L_{\text{rec}}^+, \quad (9)$$

where SSIM indicates the structural similarity (Zhou Wang et al., 2004), which is added to the L2 loss as a constraint.

Residual loss: The image outside the region of abnormality must be the same between the two types of images, $\hat{\mathbf{x}}^-$ and $\hat{\mathbf{x}}^+$, generated by the image decoder to preserve the identity between corresponding regions. Therefore, we added a loss function to guarantee the similarity between $\hat{\mathbf{x}}^-$ and $\hat{\mathbf{x}}^+$ based on the normal regions, indicated by $\overline{\mathbf{M}}$ as follows:

$$L_{\text{res}} = \|\overline{\mathbf{M}} \odot \mathbf{x}^- - \overline{\mathbf{M}} \odot \mathbf{x}^+\|_1. \quad (10)$$

Appendix D. Training Setting

All neural networks were implemented using Python 3.7 with PyTorch library 1.2.0 (Paszke et al., 2019) on an NVIDIA Tesla V100 graphics processing unit with CUDA 10.0. He initialization (He et al., 2015) was applied to both the encoder and the decoder. Adam optimization (Kingma and Ba, 2015) was used with learning rates of 5×10^{-3} . Other hyperparameters were empirically determined as follows: batch size = 240, maximum number of epochs = 300, $\lambda_1 = 1.0$, $\lambda_2 = 1.0$, $\lambda_3 = 1.0 \times 10^4$, $\lambda_4 = 1.0$, $\lambda_5 = 1.0$, and $\pi = 10.0$. The input images were grayscale two-dimensional images with the size of $1 \times 256 \times 256$. The size of latent codebook was $512 \times 64 (= K \times D)$. During training, data augmentation included horizontal flipping, random scaling, and rotation.

Appendix E. Training Results

The results of the model training at epoch 300 are shown in Figure E.1.

Appendix F. Overview of Design of Content-based Image Retrieval

An overview of the design of CBIR is presented in Figure F.1.

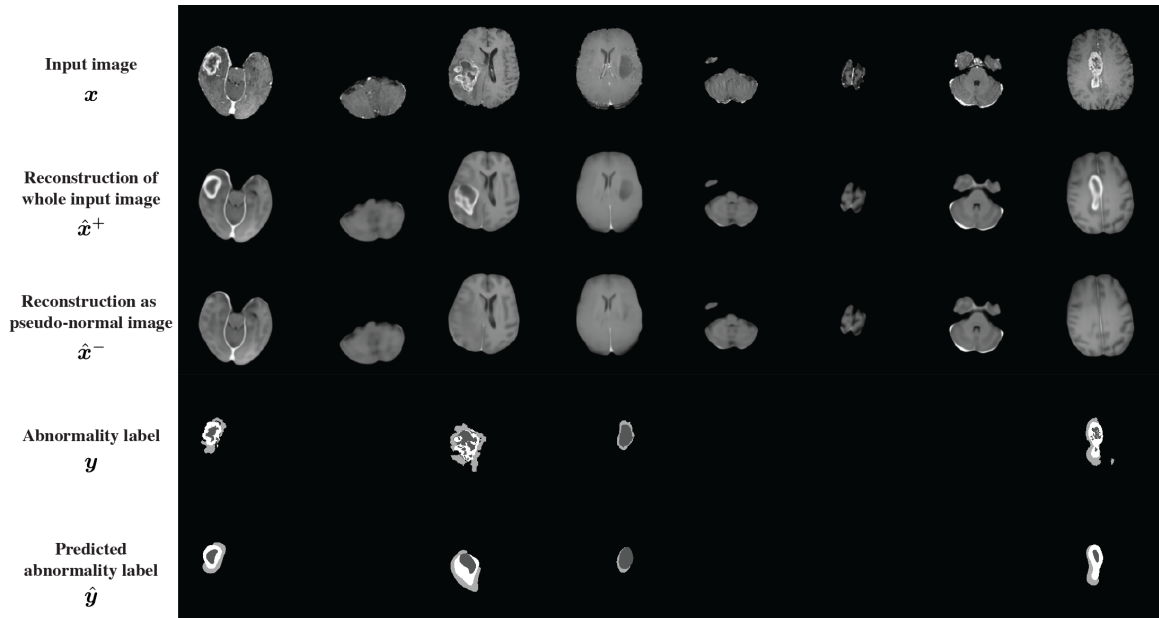


Figure E.1: Results of model training. Entire input images \hat{x}^+ (second row) were reconstructed based on both normal and abnormal anatomy codes, whereas reconstruction as pseudo-normal images \hat{x}^- (third row) were only on normal anatomy code. A clear distinction can be observed between \hat{x}^+ and \hat{x}^- at abnormal regions, which existed in both x and \hat{x}^+ but not in \hat{x}^- . The fourth and fifth rows indicate ground-truth segmentation label y for abnormality (ET, TC, and ED) and prediction for labels \hat{y} , respectively. The output of segmentation labels tended to be spherical and did not recover the detailed shape of each region. We assume this as a natural consequence since the compressed representation in the latent codes, which is advantageous for the computational cost of similarity search, did not have sufficient capacity to preserve the detailed feature in the input image as a trade-off.

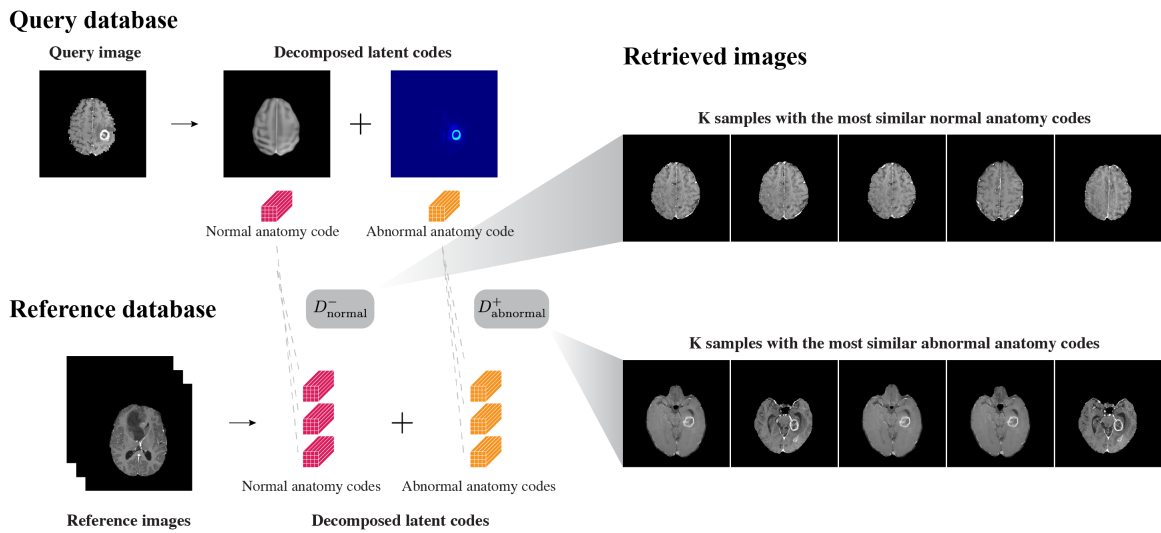


Figure F.1: Content-based image retrieval was constructed on a per-image basis, i.e., each magnetic resonance volume was separated into slices along the axial axis. From the 2019 BraTS Challenge, the validation and test datasets were used as query and reference datasets, respectively. Every image in the reference dataset was decomposed into normal and abnormal anatomy codes in advance. Furthermore, a query image was decomposed into two latent codes. Subsequently, several reference images with the most similar latent codes were extracted from the reference database.